Journal of Magnetism and Magnetic Materials 494 (2020) 165752

Contents lists available at ScienceDirect

Journal of Magnetism and Magnetic Materials

journal homepage: www.elsevier.com/locate/jmmm

Research articles

Observation of two-critical-angle phenomenon in spin wave resonances in diluted ferromagnetic semiconductor GaMnAs thin films

X. Liu[a,*], M. Dobrowolska[a], J.K. Furdyna[a], H. Puszkarski[b], P. Tomczak[b]

[a] Department of Physics, University of Notre Dame, IN 46556, USA
[b] Faculty of Physics, Adam Mickiewicz University, 61-614 Poznań, Poland

ARTICLE INFO

Keywords:
Spin wave resonance
Ferromagnetic semiconductors
Spherical surface pinning
Magnetic surface anisotropy

ABSTRACT

We have studied surface anisotropy energy and surface pinning parameters of ferromagnetic semiconductor GaMnAs film by analyzing spin wave resonance (SWR) measurements carried out on this material. The SWR spectra were observed in various polar and azimuthal angular orientations of external static magnetic field with respect to crystal axes of an annealed GaMnAs film with a Mn concentration of 8.0 at.%). The observed SWR spectra were interpreted in terms of a recently developed spherical surface pinning (SSP) theory. As predicted by the SSP theory, our data clearly show the existence of two critical angles in specific resonance configurations. The experimental confirmation of this key prediction of the SSP model brings new insights into the behavior of magnetic surface anisotropy of GaMnAs films. In particular, the agreement of our experimental results with SWR theory shows that, by including higher-order terms with cubic symmetry in the description of the surface free energy, our analysis will improve our understandings of the magnetic surface anisotropy of GaMnAs films.

1. Introduction

Ferromagnetic (FM) semiconductors have emerged as highly promising materials for semiconductor spintronic applications [1]. Among these, GaMnAs grown by low-temperature molecular beam epitaxy (MBE) is especially interesting, showing ferromagnetic properties that can be described in terms of a single-domain model characterized by well-defined cubic and uniaxial magnetocrystalline anisotropy parameters [2,3]. A full understanding of magnetic anisotropy of this material is especially important for its use in prospective spintronic applications, and is being extensively studied by a wide variety of techniques, including magnetometry, magneto-transport, ferromagnetic resonance (FMR) and spin-wave resonance (SWR) measurements [4–6].

Most of these methods have been applied to obtain information on volume properties of this material, such as bulk anisotropy fields and exchange constants. Recently, however, it has also been proposed that one can employ the full potential of SWR measurements to obtain detailed information on magnetic characteristics of the GaMnAs surface, such as magnetic surface anisotropy energy and surface pinning parameters [7]. Note that mapping of the surface anisotropy of a ferromagnetic semiconductor is an important step toward designing and building of nano-sized spintronic devices. Several early attempts [8] have already been successful in determining surface pinning parameters of GaMnAs from SWR spectra for certain angular configurations of external magnetic field $\mathbf{H_{dc}}$ by using a so-called surface inhomogeneity (SI) model [9,10]. Although in those earlier studies the surface pinning parameter A was obtained for only a limited range of field orientations, those investigations have stimulated fruitful theoretical discussion and insight [11,12].

These earlier results have also led to the development of a new and more precise theoretical model, which we will call the spherical surface pinning (SSP) model [7]. The SSP model can be applied to any ferromagnetic thin film systems which are magnetically uniform in the bulk across thin film sample. Importantly, this model has predicted the existence of two critical polar angled in SWR measurements when the magnetic field $\mathbf{H_{dc}}$ is applied along certain out-of-plane directions, a feature that has not been observed in earlier studies [13]. The observation of such double-critical-angle behavior would then constitute a full confirmation of the SSP formulation. Stimulated by these predictions, we have conducted detailed SWR measurements on a 120 nm $Ga_{0.92}Mn_{0.08}As$ film similar to that used in earlier studies [8]. SWR measurements were carried out using four basic geometries for two purposes: to confirm the existence of the newly-predicted double critical polar angle phenomenon, and to establish a procedure for mapping surface anisotropy using the SSP model, thus allowing one to explicitly account for the contribution of higher-order cubic symmetry terms to magnetic anisotropy of ferromagnetic materials.

* Corresponding author.
E-mail address: xliu2@nd.edu (X. Liu).

https://doi.org/10.1016/j.jmmm.2019.165752
Received 19 May 2019; Received in revised form 16 July 2019; Accepted 27 August 2019
Available online 03 September 2019

2. Sample preparation and experimental setup

For the purposes of this study, a 120 nm $Ga_{0.92}Mn_{0.08}As$ film was grown on (0 0 1) semi-insulating "epi-ready" GaAs substrate. Details of the growth procedure can be found in Ref. [8]. The film was annealed for one hour in N_2 gas at 310 °C [14]. Magnetic measurements carried out on the sample show a saturation magnetization $M_s = 32$ emu/cm^3 at 5 K and a Curie temperature T_C of 100.3 K, as shown in Fig. S1 in Supplementary Information. The crystalline quality of the GaMnAs epitaxial growth was examined by high resolution X-ray diffraction (HR-XRD). As shown in Fig. S2 in Supplementary Information, the HR-XRD spectrum shows a narrow GaMnAs peak with Pendellösung oscillations, indicating a homogeneous Mn distribution in the GaMnAs layer. FMR and SWR measurements were carried out using a Bruker electron paramagnetic resonance spectrometer at 9.46 GHz [2]. Detailed description of the experimental setup used in the subsequent discussion can be found in Ref. [4].

In this study we performed a complete mapping of resonance spectra as a function of magnetic field orientation, as described below. The sample was first cleaved into four square pieces with edges along [1 1 0] and [1 $\bar{1}$ 0] directions. Each square piece was then cemented to a parallelepiped of GaAs (1 0 0) in one of the four geometries shown in Fig. 1(a). In configurations 1 and 2, the GaMnAs layer was cemented with either the [1 1 0] or the [1 $\bar{1}$ 0] edge of the specimen oriented vertically. This allowed measurements with the static magnetic field $\mathbf{H_{dc}}$ applied in any intermediate direction between the normal to film, $\mathbf{H_{dc}}||[0\,0\,1]$, and the in-plane field orientation of either $\mathbf{H_{dc}}||[1\,\bar{1}\,0]$ or $\mathbf{H_{dc}}||[1\,1\,0]$ (*i.e.*, $\phi_H = -45^\circ$ or $\phi_H = 45^\circ$), respectively, as shown in Fig. 1(a). In configuration 3 the [0 1 0] crystal direction is oriented vertically, allowing us to map the SWR spectra for field orientations between $\mathbf{H_{dc}}||[0\,0\,1]$, and the in-plane field orientation $\mathbf{H_{dc}}||[1\,0\,0]$ (*i.e.*, $\phi_H = 0^\circ$). Finally, in configuration 4 the sample was mounted horizontally with the [0 0 1] direction pointing up, allowing us to map the resonance spectra with $\mathbf{H_{dc}}$ confined to the (0 0 1) plane (*i.e.*, $\theta_H = 90^\circ$) [4,7].

3. Experimental results

Fig. 2a–c show the results of SWR measurements at $T = 4$ K in geometries 2, 3 and 4, respectively. The angular dependence of SWR spectra in geometry 1 is almost identical to that observed in geometry 2. The results for this configuration are also similar to those reported in Ref. [8], and were discussed in detail there. For $\mathbf{H_{dc}}||[0\,0\,1]$ the spectrum contains at least five well-resolved bulk-type resonances separated by equal magnetic field increments. As one rotates the sample away from $\mathbf{H_{dc}}||[0\,0\,1]$, the higher-order SWR modes diminish in amplitude, and vanish altogether at a critical angle θ_c (24° in Fig. 2a), leaving only a single narrow resonance that corresponds to the uniform FMR mode. For angles $\theta_H > \theta_c$, the multi-mode resonance spectrum re-emerges, the resonance lines representing both bulk and surface modes [8,13].

The evolution of SWRs in configuration 3 (Fig. 2b) is much more complicated, displaying *two* critical angles, at $\theta_H = 20^\circ$ and 38°. This is a newly-observed phenomenon, and we elaborate on it in what follows. As one rotates the sample away from the $\mathbf{H_{dc}}||[0\,0\,1]$ orientation, the bulk-type resonance modes eventually disappear at the first critical angle $\theta_{c1} \approx 20^\circ$, at which the multi-mode spectrum transforms into a single narrow resonance line as the higher-order modes become extinguished. As θ_H increases beyond θ_{c1}, the multi-mode spectrum

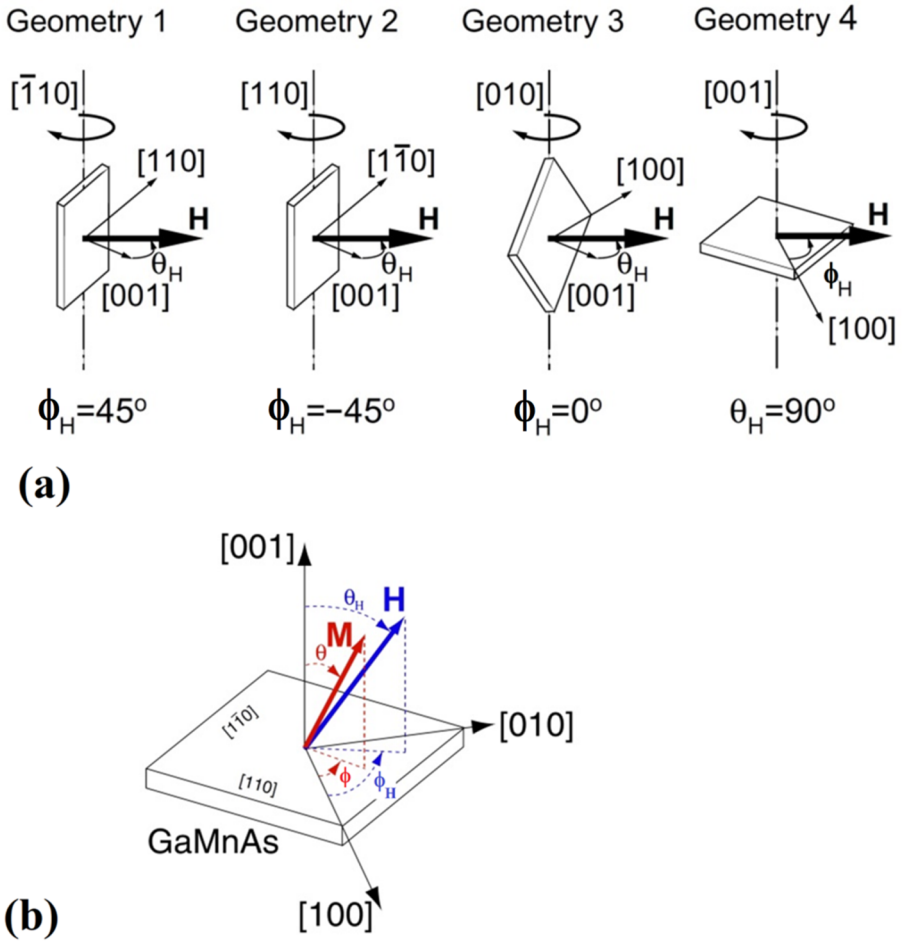

Fig. 1. (a) Schematic diagrams of the four geometries used in SWR measurements; and (b) the coordinate system used in this paper.

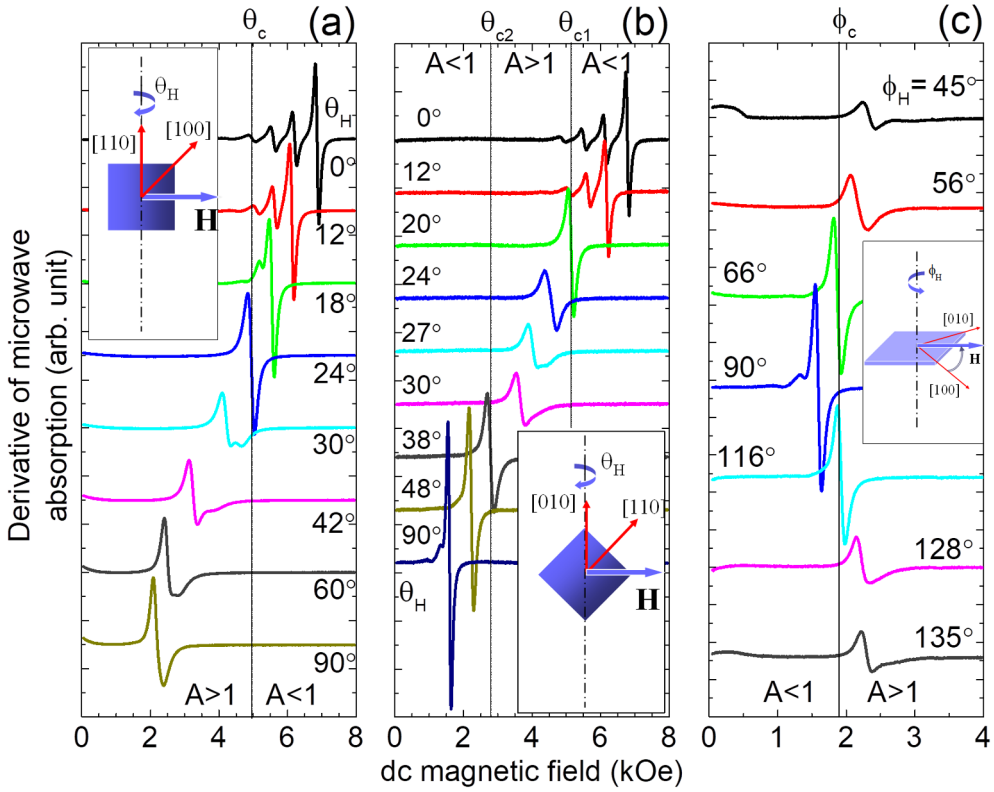

Fig. 2. Angular dependence of SWR spectra observed for the GaMnAs film at $T = 4$ K: (a) at various orientations θ_H for $\mathbf{H_{dc}}$ between [0 0 1] and [1 $\bar{1}$ 0] directions in the out-of-plane configuration ($\phi_H = -45°$); (b) at various orientations θ_H for $\mathbf{H_{dc}}$ between [0 0 1] and [1 0 0] directions in the out-of-plane configuration ($\phi_H = 0°$); and (c) at various orientations ϕ_H for $\mathbf{H_{dc}}$ in in-plane configuration ($\theta_H = 90°$).

reappears again. However, the multi-mode spectrum again transforms into a single resonance at the second critical angle, $\theta_{c2} \approx 38°$. For angles $\theta_H > \theta_{c2}$ (*i.e.,* as $\mathbf{H_{dc}}$ approaches the easy axis [1 0 0]), the spectrum gradually develops into bulk-type multi-mode SWR spectrum. Our present measurements are the first observation of such predicted double-critical-angle phenomenon [7], constituting an experimental verification of the SSP model. The results in configuration 4 (Fig. 2c) are similar to those observed in earlier studies (Fig. 3 in Ref. [8]) for the same in-plane geometry, a single resonance line occurring at ϕ_c in each quadrant (in Fig. 2c, at $\phi_c = 66°$ and 116°).

In Fig. 3, we zoom in on SWR spectra around two critical angles we observed in Fig. 2(b). Two criteria are used to identify the critical angles: 1. The spectrum at the critical angle having a single symmetric Lorentz-shape resonance line; 2. The spectrum at the critical angle having a local maximum of the peak-to-peak intensity or local minima of the peak-to-peak width. As shown in Fig. 3(a) comparison of spectra at 20° and 22° near the critical angle θ_{c1}, shows that, although both have a single Lorentz-shape resonance line, we choose 20° as the critical angle, since that spectrum has a larger peak-to-peak intensity. As shown in Fig. 3(b), around critical angle θ_{c2}, the shape of the spectra evolves from asymmetric, to symmetric, and then to asymmetric as the θ_H changes from 33° to 44°. The arrow in the figure marks the appearance of a shoulder in the spectrum at 44°. A carefully analysis of the spectra by fitting with the Lorentzian function indicates that the spectrum at 38° is more symmetric than that at 40°. Based on this, we define 38° as the critical angle.

We also plot resonance positions of SWR modes as a function of θ_H for $\mathbf{H_{dc}}$ between [0 0 1] and [1 0 0] directions in Fig. 4. In the figure, the distribution of resonance postpositions clearly shows the existence of three types of multi-mode SWR spectra observed as the angle θ_H varies from 0° to 90°, and two cross points at two critical angles. At these two critical angles the uniform resonance mode (single peak) is observed. As a result, we have demonstrated the existence of the two-critical-angle phenomenon, and determined the values of the critical angles with a precision around 2°.

4. Theory

Traditionally, the interpretation of FMR in GaMnAs is carried out in terms of the phenomenological formulation of magnetic free energy [2],

$$\begin{aligned}\frac{F}{M} = & -H(\cos\theta\cos\theta_H + \sin\theta\sin\theta_H)\cos(\phi-\phi_H) \\ & -\tfrac{1}{2}H_{2\perp}^{eff}\cos^2\theta \\ & -\tfrac{1}{4}H_{4\perp}\cos^4\theta - H_{2\parallel}\sin^2\theta\sin^2\left(\phi-\tfrac{\pi}{4}\right) \\ & -\tfrac{1}{8}H_{4\parallel}\sin^4\theta(3+\cos 4\phi).\end{aligned} \quad (1)$$

Here the first term is the Zeeman energy, $H_{2\perp}^{eff}$ represents the effective perpendicular uniaxial anisotropy field of the first order, $H_{4\perp}$ is the second order perpendicular anisotropy field, and $H_{2||}$ is the in-plane uniaxial anisotropy field. The last term accounts for the cubic anisotropy of the sample. The polar angles θ and θ_H indicate, respectively, the orientations of $\boldsymbol{M}$ and $\boldsymbol{H}$ with respect to the [0 0 1] axis, and the azimuthal orientations of $\boldsymbol{M}$ and $\boldsymbol{H}$ are given by angles ϕ and ϕ_H measured with respect to the [1 0 0] axis, as shown in Fig. 1(b). We will refer to the model described by Eq. (1) as the "first order model", and will denote it as **M1**. Recently, a more precise formulation of the free-energy density F in GaMnAs has been developed in Ref. [7], given by the following expression:

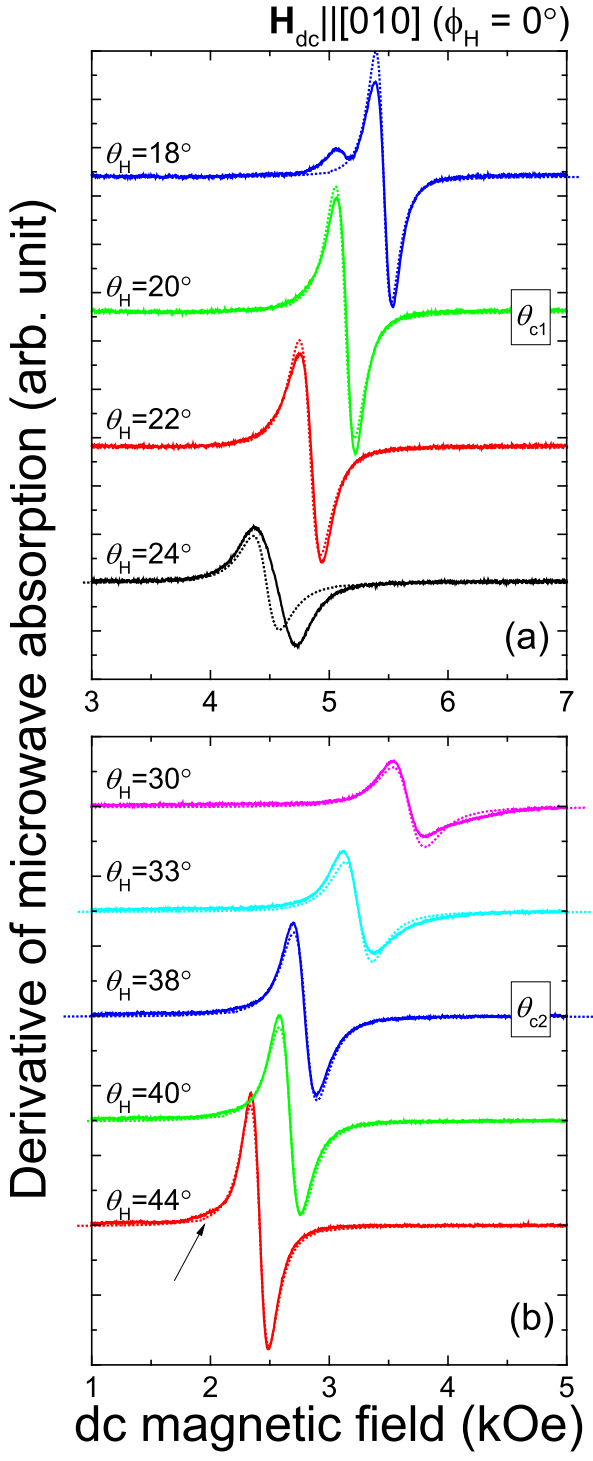

Fig. 3. Zooming-in of SWR spectra at various orientations θ_H around the two critical angles in the out-of-plane configuration ($\phi_H = 0^\circ$). The experimental data (solid) is fitted by Lorentzian curves (dashed).

$$\begin{aligned}\frac{F}{M} = & -H(\cos\theta\cos\theta_H + \sin\theta\sin\theta_H)\cos(\phi-\phi_H)\\ & -\tfrac{1}{2}H_{2\perp}^{eff}\cos^2\theta\\ & -\tfrac{1}{4}H_{4\perp}\cos^4\theta - H_{2\parallel}\sin^2\theta\sin^2\left(\phi-\tfrac{\pi}{4}\right)\\ & + H_{c1}(n_x^2n_y^2 + n_y^2n_z^2 + n_z^2n_x^2) + H_{c2}(n_x^2n_y^2n_z^2)\\ & + H_{c3}(n_x^4n_y^4 + n_y^4n_z^4 + n_z^4n_x^4)\\ & + H_{c4}(n_x^4n_y^4n_z^2 + n_x^4n_y^2n_z^4 + n_x^2n_y^4n_z^4). \end{aligned} \quad (2)$$

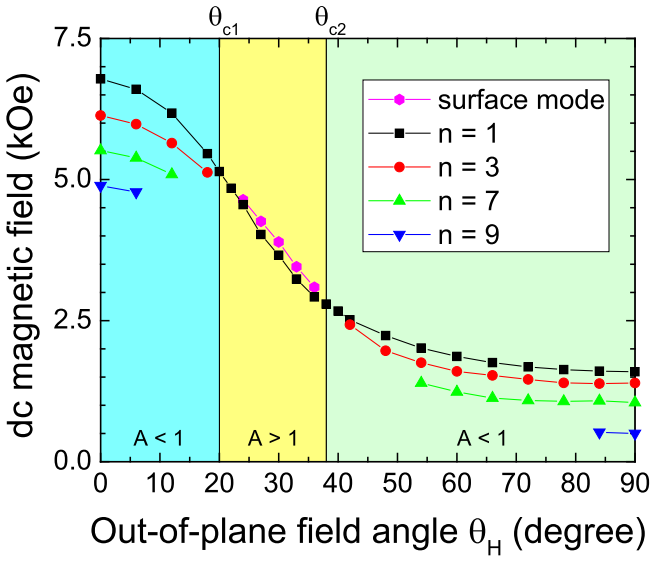

Fig. 4. (a) Angular dependence of SWR modes observed for the GaMnAs film at $T = 4$ K at various orientations θ_H for $\mathbf{H_{dc}}$ between [0 0 1] and [1 0 0] directions in the out-of-plane configuration ($\phi_H = 0^\circ$).

We will refer to this formulation as the "extended model" **M2**. The **M2** model differs from **M1** in how it takes into account the magnetic cubic anisotropy. In model **M1**, cubic anisotropy is simply represented by the term $H_{4\parallel}$, whereas in **M2** the contribution of cubic symmetry to F/M is expanded in Eq. (2) as a superposition of terms originating from fields H_{c1}, H_{c2}, H_{c3}, H_{c4}, as discussed in Ref. [7], Eqs. (1) and (2). The Zeeman and uniaxial anisotropy contributions in **M1** are the same as in **M2**.

Additionally, in earlier papers [11,12] some of us have shown that in order to obtain a full understanding of spin wave excitations in ferromagnetic thin films, it is necessary to also include the contribution of free energy associated with magnetic surface anisotropy. This was accomplished by formulating the so-called surface inhomogeneity (SI) model, which describes spin wave excitations in a ferromagnetic film by truncating the homogeneity of magnetic properties in the form of discontinuities at surfaces. The spin wave behavior of the system can then be formulated by introducing a surface pinning parameter A [9,10], defined as:

$$A = 1 - \frac{d^2}{D_{ex}}\boldsymbol{K}_{eff}^{surf}\cdot\hat{\boldsymbol{m}} \quad (3)$$

where D_{ex} is the exchange constant (both bulk and surface), d is the lattice constant of magnetic ions, $\hat{\boldsymbol{m}}$ represents the unit vector of the magnetization of the film, and $\boldsymbol{K}_{eff}^{surf}$ is referred to as the effective surface anisotropy field. The field $\boldsymbol{K}_{eff}^{surf}$ is understood as a phenomenological quantity that accounts for the difference between the "pinning" of surface and bulk spins, as discussed in detail in Refs. [9] and [10]. In terms of view of free-energy density, the value of A is represented by [7,15]

$$A = 1 + \frac{d^2}{MD_{ex}}[F^{surf} - F^{bulk}] \quad (4)$$

where F^{surf} and F^{bulk} are the free-energy densities of surface and bulk spins, respectively. The parameter A can now be expressed in terms of models **M1** and **M2** described earlier, thus generalizing these models to include the effects of the surface. We will refer to the models so generalized as **SM1** and **SM2**, respectively. In the **SM1** model, A now reads

$$A(\theta_H,\phi_H) = 1 + a_{iso} - \tfrac{1}{2}A_{2\perp}\cos^2\theta - \tfrac{1}{4}A_{4\perp}\cos^4\theta - A_{2\parallel}\sin^2\theta\sin^2\left(\phi - \tfrac{\pi}{4}\right) - \tfrac{1}{8}A_{4\parallel}\sin^4\theta(3 + \cos 4\phi) \quad (5)$$

Similarly, in the model **SM2**, corresponding to model **M2**, A can be written as,

$$A(\theta_H,\phi_H) = 1 + a_{iso} - \tfrac{1}{2}A_{2\perp}\cos^2\theta - \tfrac{1}{4}A_{4\perp}\cos^4\theta - A_{2\parallel}\sin^2\theta\sin^2\left(\phi - \tfrac{\pi}{4}\right) + A_{c1}(n_x^2n_y^2 + n_y^2n_z^2 + n_z^2n_x^2) + A_{c2}(n_x^2n_y^2n_z^2) + A_{c4}(n_x^4n_y^4n_z^2 + n_x^4n_y^2n_z^4 + n_x^2n_y^4n_z^4) \quad (6)$$

Note that the term A_{c3} is absent in the **SM2** model since, as will be explained later, including it in Eq. (6), leads to overfitting (see discussion of a similar issue concerning bulk anisotropy [16]). Importantly, by experimental mapping of the pinning parameter A at various polar and azimuth angles, we can obtain pinning energy densities for surface spins, as shown in the next Section.

5. Theory *versus* SWR experiment

In order to fully understand the effect of surfaces in GaMnAs films as they relate to SWR, one can map the behavior of parameter A as a function of magnetization orientation. As introduced in earlier literature [10], A identifies the wave vector k and the amplitude for each SWR mode, as well as the separation between the first two (surface and bulk) spin wave modes when $A > 1$ [9,10]. Thus, by carefully fitting the SWR spectra by multiple Lorenz peaks, we can quantify the value of A with an error of around 1% as a function of orientation (θ_H, ϕ_H) of the applied field $\mathbf{H_{dc}}$.

The experimental results for all four geometries used in our SWR measurements are shown in Fig. 5 as blue square symbols. Note that we cannot obtain reliable values of A when only bulk-type spin wave modes are present (*i.e.*, in the region $A < 1$), since in that case A has little effect on the SWR peak intensities. In Fig. 5 we show results of application of **SM1** and **SM2** models to fit available experimental data. To avoid overfitting, we have used the cross-validation procedure described in Ref. [16] to find the pinning parameters in Eqs. (5) and (6). The best fits for both models are plotted in the figure, with the corresponding fitting parameters listed in Tables 1 and 2. Both fits present the experimental results quite reasonably. The function $\langle E^1_{RMS}\rangle$, as defined in Ref. [16], measures the ability to predict new data resulting from the given model – if its value was zero, the model prediction would be accurate. Therefore, we see that the model **SM2** has a better predictive ability than the **SM1** model. In particular, the **SM2** model fits the critical points for all geometries much better than **SM1**, as can be seen from Table 3.

Table 1
Surface pinning parameters obtained from model "**SM1**". The definition of $\langle E^1_{RMS}\rangle$, an error function, the positive square root of the sum of squares of residuals, is given in Ref. [16].

$A_{4\parallel}$	$A_{2\perp}$	$A_{4\perp}$	$A_{2\parallel}$	a_{iso}	$\langle E^1_{RMS}\rangle$
0.2541	−0.1130	1.351	0.004603	0.1038	0.01392

Table 2
Surface pinning parameters obtained from model "**SM2**". The definition of $\langle E^1_{RMS}\rangle$, an error function, the positive square root of the sum of squares of residuals, is given in Ref. [16].

A_{c1}	A_{c2}	A_{c4}	$A_{2\perp}$	$A_{4\perp}$	$A_{2\parallel}$	a_{iso}	$\langle E^1_{RMS}\rangle$
0.4027	−2.793	5.168	−0.4000	−1.800	0.01018	−0.05962	0.01250

In Fig. 6 we plot color maps resulting from our SSP model for both **SM1** and **SM2**, calculated using the pinning coefficients shown in Tables 1 and 2. In particular, Fig. 6 maps the conditions for the existence of surface modes for the (θ_H, ϕ_H) plane of the GaMnAs sample investigated in this work. In Fig. 6, the white areas indicate regions where $A < 1$; blue areas are for $A > 1$; and the borders between blue and white areas indicate the conditions where A equals unity, *i.e.*,

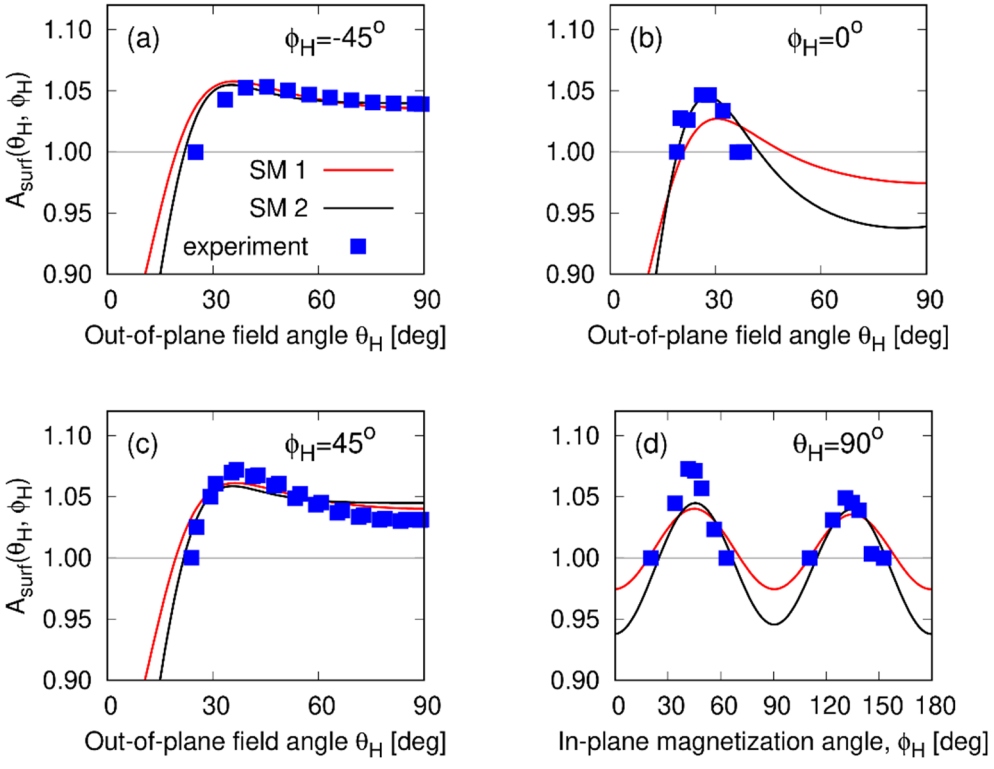

Fig. 5. Dependence of the surface pinning parameter A on *dc* field orientation (solid lines) according to our two SSP models in the four configurations used in our measurements, compared with experimental points (blue squares). The two sets of data in (a)(b)(c) are for θ_H and $-\theta_H$, respectively. In principle, the SWR modes should be symmetric with respect to 0° due to mirror symmetry. The difference is due to experimental error. The error bars are within the square symbols in the figure. (For interpretation of the references to color in this figure legend, the reader is referred to the web version of this article.)

Table 3
Critical angles: experiment vs. theory.

	Geometry 2 (out-of-plane)	Geometry 3 (out-of-plane)		Geometry 4 (in-plane)	
Experiment	$\theta_c = 24^\circ$	$\theta_{c1} = 20^\circ$	$\theta_{c2} = 38^\circ$	$\phi_c = 66^\circ$	$\phi_c = 116^\circ$
Theory – SM1	20°	21°	49°	71°	111°
Theory – SM2	22°	19°	42°	65°	115°

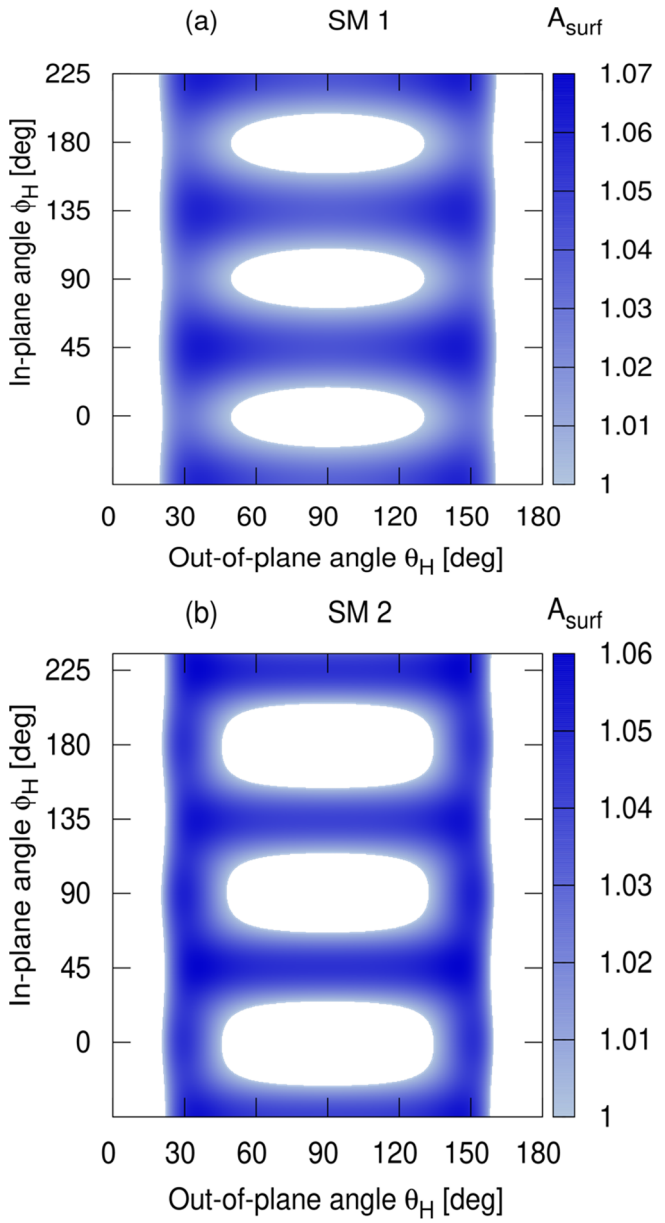

Fig. 6. Spherical contour plots for bulk and surface spin wave modes according to the SM1 model (a) and SM2 model (b). Blue regions are regions in the (θ_H, ϕ_H) plane where surface SWR modes will occur, since in these regions the value of surface parameter is greater than one ($A > 1$). The value of A is less than one ($A < 1$) in the white areas, indicating conditions where bulk SWR modes are present. At the contour boundaries of the blue area $A = 1$, indicating conditions for critical pinning, $k = 0$, as discussed in Ref. [7]. (For interpretation of the references to color in this figure legend, the reader is referred to the web version of this article.)

where critical angles occur. The color-bar next to the figure indicates numerical values of A in the color map. We recall that surface spin wave modes can only exist in regions when $A > 1$. Thus the edges of the blue areas define the sets of *critical angle* configurations in which the spectrum of multiple SWRs reduces to a single resonance, as predicted by both models.

We now correlate these maps with the results shown in Fig. 2. The SWR spectra obtained for various values of θ_H in the $\phi_H = -45^\circ$ plane (Fig. 2a) correspond to moving horizontally *at* $\phi_H = -45^\circ$ in Fig. 4. As we increase θ_H in that plane, at $\theta_H \approx 24^\circ$ we will cross the boundary between the white and the blue zones, entering the regime where bulk SWs cease to exist, and surface SWs begin to form. Proceeding horizontally with increasing θ_H, we remain in the regime where surface conditions for surface SWs continue to be fulfilled, all the way to $\theta_H = 90^\circ$, as is indeed confirmed by experiment. The situation is, however, very different when θ_H is varied in the $\phi_H = 0$ plane, corresponding to Fig. 2b. In this case, as we move horizontally at $\phi_H = 0^\circ$ starting at $\theta_H = 0^\circ$ in Fig. 6 (where $A < 1$, *i.e.*, where bulk SWs are observed), we first cross the blue/white boundary at that critical angle $\theta_{c1} \approx 20^\circ$ and enter the zone of $A = 1$, where conditions for surface SWs are satisfied. Importantly, however, as θ_H is increased further, we exit these conditions at another critical angle $\theta_{c2} \approx 38^\circ$, and re-enter the colored zone ($A < 1$) where surface spin waves transform to bulk waves. Our SWR results reveal that for fields applied in the $\phi_H = 0^\circ$ plane two critical angles, at $\theta_{c1} \approx 20^\circ$ and $\theta_{c2} \approx 38^\circ$ indeed exist, thus confirming the predictions of the SSP model. Summarizing the insights provided by Fig. 4, the critical polar angle θ_{c1} can be observed at all values of the azimuthal angle (*i.e.*, in all out-of-plane configurations); but, in contrast, critical angle θ_{c2} is very sensitive to ϕ_H, and can only be observed in very limited angular ranges around $\phi_H = 0^\circ$ and $\phi_H = 90^\circ$. Outside of these ranges, only one critical polar angle can be found in out-of-plane configurations. Finally, by comparing experimental results at critical angles for the two models (see Table 3 and Fig. 6), we find that this critical feature is more correctly represented by model **SM2**.

6. Mapping of surface pinning terms

Let us finally analyze the individual pinning terms in the expressions for the pinning parameters in the **SM1** and **SM2** models, Eqs. (5) and (6) by mapping their contributions in spherical coordinates. In Fig. 7 we plotted hypersurfaces for different pinning terms – as indicated on the graphs – and for the resulting total pinning parameter. As one can see, the main difference between models **SM1** and **SM2** arises from the cubic symmetry term in the pinning energy expansion. Note, however, that in both models the [0 0 1] crystal axis is the "strong" surface pinning direction, whereas axes [1 0 0] and [0 1 0] are "weak" axes.

In Fig. S3 we have also plotted the angular dependences of the surface spin pinning parameter A in the (θ_H, ϕ_H) plane that result from our two SSP models, with experimental data shown as red squares. It is clearly seen that $A(\theta_H, \phi_H)$ has a four-fold symmetry with respect to ϕ_H, and a two-fold symmetry with respect to θ_H. This behavior is of course expected from the angular dependence of the free energy density F, see Eqs. (1) and (2), since the pinning hypersurface graphically expresses the co-existence of cubic and uniaxial anisotropy contributions. One should note, however, that without the cubic contribution no critical angles could exist in the in-plane configuration. Additionally, the observation of two critical polar angles, θ_{c1} and θ_{c2}, provides indisputable evidence that cubic surface anisotropy contributes significantly to the process of surface pinning in GaMnAs films.

7. Concluding remarks

It should be mentioned that the GaMnAs film studied in this work is not an isolated case showing the existence of the two-critical-angle phenomenon. In Supplementary Information, Figs. S4–S7, we show

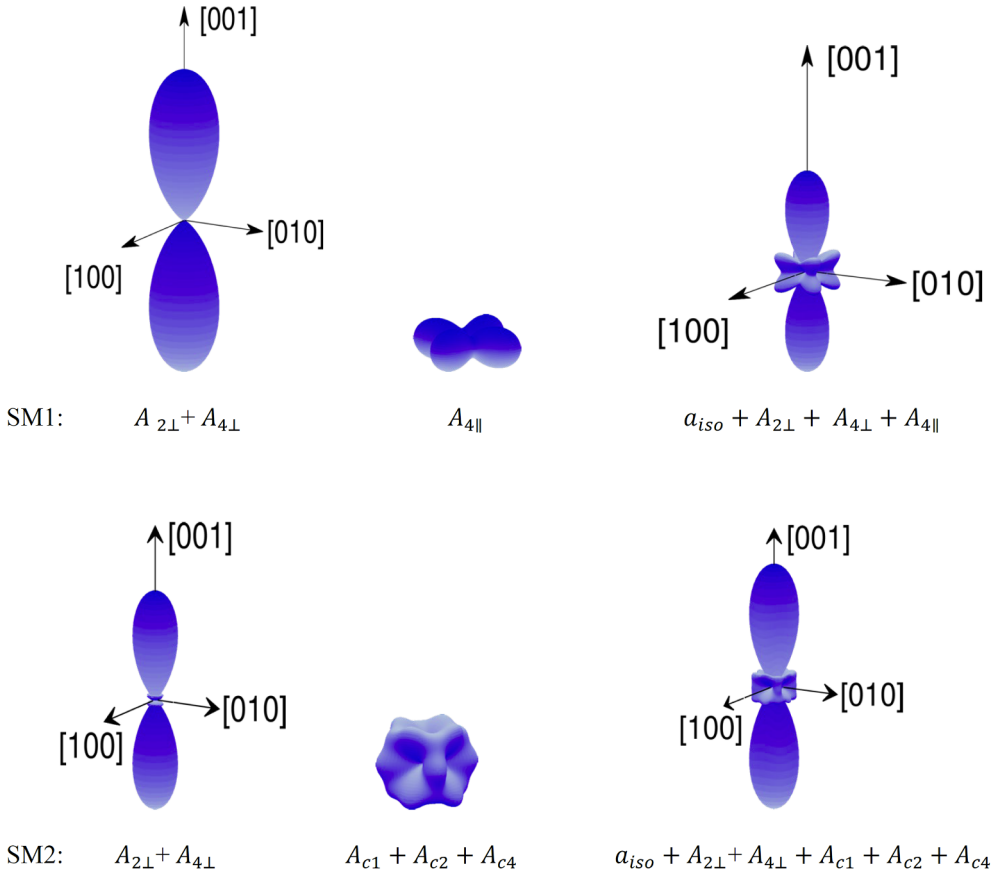

Fig. 7. Surface pinning terms in spherical coordinates, as discussed in the text, see Eqs. (5) and (6). Top row corresponds to the SM1 model, where $A_{2\perp} + A_{4\perp}$ represent the pinning term resulting only from perpendicular anisotropy; $A_{4\parallel}$ represents pinning due to cubic anisotropy; and $a_{iso} + A_{2\perp} + A_{4\perp} + A_{4\parallel}$ is total pinning. Bottom row shows the same results calculated with model SM2, where $A_{2\perp} + A_{4\perp}$ is the pinning term due only to from perpendicular anisotropy; $A_{c1} + A_{c2} + A_{c4}$ represents pinning due to cubic anisotropy; and $a_{iso} + A_{2\perp} + A_{4\perp} + A_{c1} + A_{c2} + A_{c4}$ is the total surface pinning. The parameter a_{iso} stands for the dimensionless surface pinning constant (see Eq. (4.9) in Ref. [7]); its values for both models are given in Tables 1 and 2. In both models the [1 0 0], [0 1 0] are "weak" axes of surface pinning, whereas [0 0 1] is the "strong" axis.

SWR data observed in another GaMnAs film, demonstrating same phenomenon in the same configuration. These results indicate that the effect of surface anisotropy and the angular dependence of pinning conditions are an intrinsic property of GaMnAs films, and that the analysis used in this work can be therefore applied to other magnetic films. In addition, as shown in Fig. 8, a critical temperature at $T_s = 15$ K is also observed, showing a uniform mode for $\mathbf{H_{dc}}||[1\,0\,0]$. As a result, at the temperature above the critical temperature, the two-critical-angle phenomenon disappears, and only a single critical angle phenomenon is observed in all four configurations. It is well known that the in-plane cubic anisotropy in GaMnAs decreases faster than the in-plane uniaxial anisotropy as the temperature increases, while the biaxially-magnetized domains make a transition to uniaxial domains. We therefore suggest that the observed the critical temperature and the disappearance of the two-critical-angle phenomenon are related to the decrease of cubic anisotropy terms (both surface and bulk).

Note that several previous reports suggested that the magnetic properties of GaMnAs film are not fully homogeneous along the growth direction [17,18], and that the boundary conditions could be different for the top and bottom surfaces of the film. Resonance spectra and the analysis in this work might shed light on assessing the magnetic uniformity and boundary conditions of the film. The fact that SWR spectra reveal the existence of the critical angle phenomenon is consistent with that the homogeneity of the sample meets the assumptions of the SI model. This is based on the interpretation of the quantum theory of SWR [9,10], according to which the critical angle occurs only in the SI model, because this phenomenon is strictly a surface effect. It occurs only when surface pinning allows a reduction of its strength to the level of natural pinning in a certain strictly defined angular configuration, which is called the critical angle configuration. Furthermore, it should be pointed out that there are no signs of the boundary asymmetry [10] from the observed SWR spectra – a single Lorentz-shape spectrum is observed at all critical angles. Finally, note that a certain volume inhomogeneity can appear in GaMnAs film in some range of angles, *i.e.*, in configurations close to the perpendicular configuration ($\theta_H = 0$). For these configurations surface pinning is very strong ($A < 1$), and such pinning, as was shown in an earlier work [11], is accompanied by a large value of *surface* exchange length. Due to such increase of the exchange length, the strong surface pinning induces a certain degree of magnetic inhomogeneity in the near-surface region of the sample.

In conclusion, mapping SWR spectra in all four configurations investigated in this paper has revealed the existence of two critical angles in specific angular configurations investigated experimentally in this paper. This observation verifies the SSP model of SWR, bringing new insights to surface phenomena in GaMnAs films, and providing information that will be of interest in designing spintronic devices. In this context the agreement of our experimental results with SWR theory shows that, by including higher-order terms with cubic symmetry in the

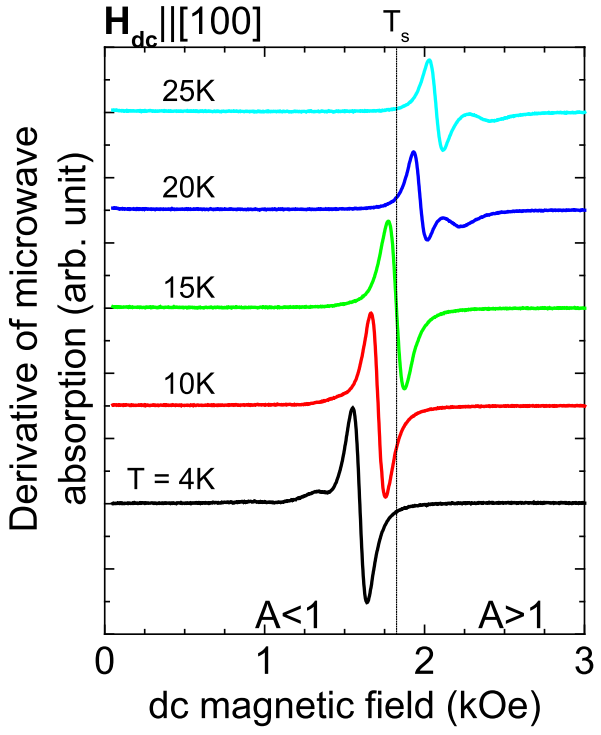

Fig. 8. SWR spectra observed at various temperatures at $\mathbf{H_{dc}}||[1\,0\,0]$. These results suggest the disappearance of the double critical angles as the temperature exceeds 15 K.

description of the surface free energy, our analysis will improve our understandings of the magnetic surface anisotropy of GaMnAs films.

Declaration of Competing Interest

No conflict of interest.

Acknowledgements

The work at University of Notre Dame was supported by the NSF Grant DMR14-00432; and at Adam Mickiewicz University by the Narodowe Centrum Nauki (National Science Center) under Grant No. DEC-2013/08/M/ST3/00967.

Appendix A. Supplementary data

Supplementary data to this article can be found online at https://doi.org/10.1016/j.jmmm.2019.165752.

References

[1] T. Janda, P.E. Roy, R.M. Otxoa, Z. Šobáň, A. Ramsay, A.C. Irvine, F. Trojanek, M. Surýnek, R.P. Campion, B.L. Gallagher, P. Němec, T. Jungwirth, J. Wunderlich, Nat. Commun. 8 (2017) 15226.
[2] X. Liu, Y. Sasaki, J.K. Furdyna, Phys. Rev. B 67 (2003) 205204.
[3] U. Welp, V.K. Vlasko-Vlasov, X. Liu, J.K. Furdyna, T. Wojtowicz, Phys. Rev. Lett. 90 (2003) 167206.
[4] X. Liu, J.K. Furdyna, J. Phys.: Condens. Matter 18 (13) (2006) R245.
[5] A. Ben Hamida, S. Sievers, K. Pierz, H.W. Schumacher, J. Appl. Phys. 114 (2013) 123704.
[6] L. Dreher, C. Bihler, E. Peiner, A. Waag, W. Schoch, W. Limmer, S.T.B. Goennenwein, M.S. Brandt, Phys. Rev. B 87 (2013) 224422.
[7] H. Puszkarski, P. Tomczak, Surf. Sci. Rep. 72 (2017) 351–367.
[8] X. Liu, Y.Y. Zhou, J.K. Furdyna, Phys. Rev. B 75 (2007) 195220.
[9] H. Puszkarski, Acta Phys. Polonica A 38 (1970) 217 **38**, 899 (1970).
[10] H. Puszkarski, Prog. Surf. Sci. 9 (1979) 191.
[11] H. Puszkarski, P. Tomczak, Sci. Rep. 4 (2014) 6135.
[12] H. Puszkarski, P. Tomczak, H.T. Diep, Phys. Rev. B 94 (19) (2016) 195303.
[13] J.T. Yu, R.A. Turk, P.E. Wigen, Phys. Rev. B 11 (1975) 420.
[14] I. Kuryliszyn, T. Wojtowicz, X. Liu, J.K. Furdyna, W. Dobrowolski, J.-M. Broto, M. Goiran, O. Portugall, H. Rakoto, B. Raquet, arXiv preprint cond-mat/0206371, 2002.
[15] H. Puszkarski, Acta Phys. Polonica A129 (2016) RK.129.6.1-1.
[16] P. Tomczak, H. Puszkarski, Phys. Rev. B 98 (2018) 144415.
[17] S.T.B. Goennenwein, T. Graf, T. Wassner, M.S. Brandt, M. Stutzmann, J.B. Philipp, R. Gross, M. Krieger, K. Zürn, P. Ziemann, A. Koeder, S. Frank, W. Schoch, A. Waag, Appl. Phys. Lett. 82 (2003) 730.
[18] P. Němec, V. Novák, N. Tesařová, E. Rozkotová, H. Reichlová, D. Butkovičová, F. Trojánek, K. Olejník, P. Malý, R.P. Campion, B.L. Gallagher, Jairo Sinova, T. Jungwirth, Nat. Commun. 4 (2013) 1422.